

Article

Not peer-reviewed version

Effect of the Molybdenum Content on Wear and Corrosion Behavior of Fe-B Based Surface Alloyed Layer

[Engin Kocaman](#) *

Posted Date: 15 November 2023

doi: 10.20944/preprints202311.0978.v1

Keywords: Hardfacing; Surface alloying; Hardness; Wear; Corrosion



Preprints.org is a free multidiscipline platform providing preprint service that is dedicated to making early versions of research outputs permanently available and citable. Preprints posted at Preprints.org appear in Web of Science, Crossref, Google Scholar, Scilit, Europe PMC.

Copyright: This is an open access article distributed under the Creative Commons Attribution License which permits unrestricted use, distribution, and reproduction in any medium, provided the original work is properly cited.

Disclaimer/Publisher's Note: The statements, opinions, and data contained in all publications are solely those of the individual author(s) and contributor(s) and not of MDPI and/or the editor(s). MDPI and/or the editor(s) disclaim responsibility for any injury to people or property resulting from any ideas, methods, instructions, or products referred to in the content.

Article

Effect of the Molybdenum Content on Wear and Corrosion Behavior of Fe-B Based Surface Alloyed Layer

Engin Kocaman *

1Zonguldak Bülent Ecevit University, Faculty of Engineering, Department of Aerospace Engineering, İncivez, 67100, Zonguldak, Türkiye; enginkocaman@beun.edu.tr

Abstract: In this study, Fe-Mo-B based hardfacing electrodes containing different amounts of Mo were coated on an AISI 1020 steel substrate using the electric arc welding method. The findings show that molybdenum is highly effective on the microstructure and minor changes in the coating composition affect the phases and morphological properties. In the hardness tests, an increase of 73% was achieved in the $Fe_{14}Mo_2B_4$ based hardfacing coating compared to the base material and a 30% increase compared to the $Fe_{16}B_4$ based coating. The highest macro hardness value was measured as 56.4 HRC and the highest phase hardness was measured as 3228 HV in the $FeMo_2B_2$ phase. The lowest wear rate was measured in the $Fe_{14}Mo_2B_2$ based coating. The wear rate of the $Fe_{14}Mo_2B_4$ based coating was 8.1 times lower than that of the substrate material and 4.7 times lower than that of the $Fe_{16}B_4$ based coating. According to corrosion test results, the highest corrosion resistance was obtained in $Fe_{16}B_4$ based coating. The current density value of the $Fe_{16}B_4$ based coating was measured to be 13.6 times lower than that of the substrate material

Keywords: hardfacing; Surface alloying; hardness; wear; corrosion

1. Introduction

Steel is one of the most important metals owing to its wide range of uses, from structural applications to automotive, aerospace, and shipbuilding industries [1–4]. The reason why Steel is an important metal because of its mechanical properties such as high strength, high toughness, and relatively easy production and processing [5]. However, most steels particularly carbon steels cannot exhibit sufficient performance under service conditions where high wear resistance and corrosion resistance are required [6,7]. In today's industrial conditions, interest in materials that exhibit high performance is increasing day by day. At this point, researchers are making intense efforts to improve the properties of the material. In service conditions where the use of steel is inevitable, improving the surface properties instead of improving the properties of the entire material appears to be a very economical engineering approach [8,9].

Although the surface properties of steel materials can be improved by various methods, hardfacing coatings are a good alternative, especially in aggressive working conditions, such as mining and excavation, where the material is exposed to high wear and corrosion. In hardfacing coatings, the surface of the material is coated with a material that provides high performance using a suitable welding method [10]. Various welding methods such as shielded manual arc welding (SMAW) [11], flux cored arc welding (FCAW) [12], plasma transfer arc welding (PTA) [13], gas tungsten arc welding (GTAW) [14] and laser welding (LW) [15,16] are used in hardfacing applications. Although these methods have advantages and disadvantages compared to each other, they are widely used in SMAW hardfacing applications because the process is economical and simple. Many alloy compositions are used as coating materials in the hardfacing process. Nowadays, it is seen that coating materials containing carbides and borides formed by transition metals such as Cr, Ti, V, Nb and Mn are frequently used. One of the transition metal molybdenum is an element that can contribute to the improvement of material surface properties by in-situ forming boride and carbide phases on the coating surface. There are various studies in the literature where molybdenum

is used as a coating material. There are many studies in which molybdenum is used as a coating material. In these studies, it is generally seen that the wear or corrosion properties on the surface are improved after hardfacing [17–20]. On the other hand, some studies have reported that molybdenum increases corrosion resistance in the presence of an element such as chromium or nickel, but its effect alone is still unclear [21,22]. It is seen in the literature that hardfacing coating studies carried out with molybdenum-containing compounds focus mostly on wear. The studies performed with Fe-Mo-B based hardfacing coatings are very limited, especially the studies examining the microstructures formed in varying molybdenum ratios and the corrosion behavior of the coating. The effect of molybdenum is unclear in some studies reveals that there are not enough studies on Fe-Mo-B based coatings. In this study, Fe-Mo-B based hardfacing electrodes containing different amounts of molybdenum were produced and coated on an AISI 1020 steel substrate using the electric arc welding method. Microstructural investigations, hardness test, wear and corrosion resistance of the coated samples were comparatively examined with substrate metal and Fe-B based coating.

2. Experimental Procedure

In the experimental studies, hardfacing electrodes containing different ratios of Fe-Mo-B were produced. In the production of hardfacing electrodes, H08A low carbon wire rod steel wire was used as the core metal, and ferromolybdenum, ferroboron, flux material (5%) and binder potassium silicate (17.5%) were used in the cover composition. The chemical compositions of ferro alloy powders and core metal are given in Table 1.

Table 1. Compositions of powders used in experimental studies (wt.%).

	C	Cr	Mo	B	Mn	Si	P	S	Fe
H08A	<0,1	0,064	-	-	0,35-0,40	0,10	<0,02	<0,02	Bal.
AISI 1020	0,22	0,025	0,02	-	0,52	0,17	0,023	0,019	Bal.
Ferro-Mo	-	-	60	-	-	1,5	0,050	0,10	38,35
Ferro -B	0,312	-		18,58		0,39	0,029	0,003	80,602

Covered electrodes were weighed by calculating their atomic ratios according to the compositions given in Table 2, and the powders were first mixed wet by adding binder and then mixed as dry. The covering paste in the viscose form was pressed in a PTFE-coated aluminum mold and the core metal was passed through it. Atomic calculation of the electrode compositions and details of the production process can be found in previous studies carried by Kocaman et al. [23,24]. The coating process was carried out using an electric arc welding machine at 125 A (amperes) and 25 V (volts) constant potential, on the AISI 1020 steel substrate, whose chemical composition is given in Table 1.

Table 2. Chemical composition of electrodes cover (at.%).

Compound	B	Mo	Fe
Fe ₁₆ B ₄	20	-	Bal.
Fe ₁₅ MoB ₄	20	5	Bal.
Fe ₁₄ Mo ₂ B ₄	20	10	Bal.
Fe ₁₄ Mo ₄ B ₂	10	20	Bal.

The coated samples were cut, subjected to standard metallographic operations, and their surfaces were sanded and polished, as can be seen in Figure 1. The samples to be used for microstructural examinations were etched using 4% Nital solution. The surface morphology and elemental distribution of the samples were analyzed using the JEOL-JSM-6060 scanning electron microscope (SEM) and X-ray spectroscopy (EDS) device coupled to the scanning electron microscope. The phases in the microstructure were analyzed with Rigaku brand X-Ray diffraction analysis (XRD) and defined using the X-pert High score program.

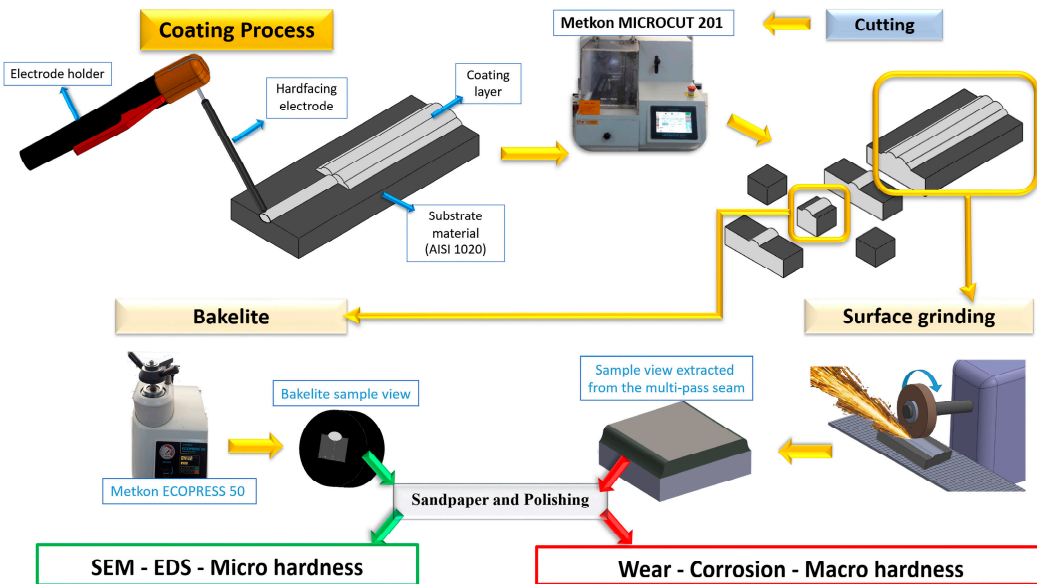


Figure 1. Schematic illustration of production processes.

Macro hardness measurements of hardfacing coatings were carried out with Bulut Makina DIGIROCK RB model hardness device. Shimadzu HMV-G21D Vickers microhardness device was used for micro hardness measurements. Dry sliding wear test was performed TriboTechnic wear device with reciprocating wear mode against a Al_2O_3 (2050 HV) ball with 10 mm dimensions. Wear tests were carried out at two different loads, 4 N and 8 N, and at two different wear distances, 400 m and 800 m. Following the wear tests, the area of wear tracks was measured using a Taylor Hobson 2D profilometer. All wear tests were performed at constant humidity (31-34%) and room temperature (23-25 $^{\circ}\text{C}$). Friction coefficient (FC) data was provided by a computer software connected to the wear device and was calculated according to the following formula.

$$FC = \frac{F_s}{F_N} \quad (1)$$

In the formula F_s represents the lateral load (N) and F_N normal load.

The wear rate was calculated according to the formula [25] below, using the data obtained from the wear tracks measurement.

$$WR = V/S \quad (2)$$

where, V is the wear trace volume and S is the sliding distance.

Gamry 1010 E potansiyotat electrochemical work station equipped with a classic three-electrode system was used during electrochemical tests. Saturated calomel electrode (SCE) reference electrode and graphite counter electrode was used corrosion tests. Open circuit potential (OCP) was measured during 1200 sec. The tests were performed in 0.5M NaCl solution with a potential range -0.5 V, +1.5 V and scanning rate was chosen as 1 mV/sec. E_{cor} (corrosion potential) and I_{cor} (corrosion current) were calculated by using Gamry Echem software. Electrochemical impedance spectroscopy (EIS) tests were performed with alternative current signal of 10 mV and the range of 100 kHz to 10 mHz.

3. Results

3.1. Microstructure and Phases Analysis

Figure 2 shows the substrate-coating transition zone of hardfacing coatings. One of the most important features that distinguish hard coating from other coating methods is that their coating thickness is quite high and they create strong metallurgical bonds with the substrate. These features enable hardfacing coatings to be used for a long time in aggressive environments. On the other hand, porosities that will occur in the transition zone and coating layer after coating will significantly reduce the performance of the coating. SEM images show that the alloys selected as the coating material and the process are compatible and a metallurgical bond is formed between the substrate material and the coating layer. Additionally, no significant porosity formation was observed in either the transition zone or the coating layer. In the SEM images, the coating process carried out at room temperature, columnar grains were formed at the interface, extending from the substrate material towards the coating area. During repeated melting and solidification, the temperature increases and columnar grains grow from the colder substrate material towards the coating region. The interface, which develops depending on the dynamic solidification conditions of the welding process, has been reported in similar studies [17,23].

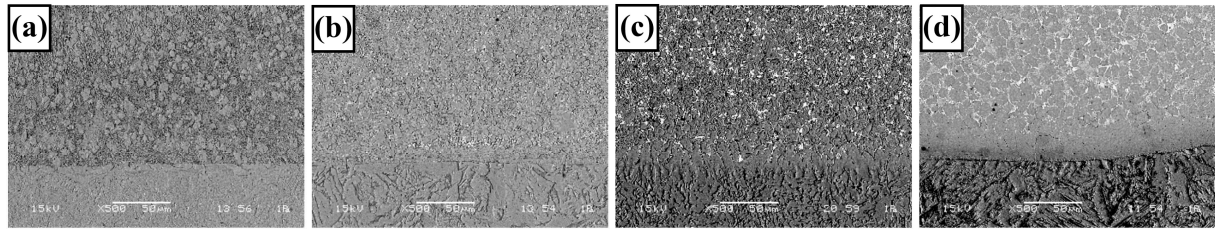


Figure 2. SEM images of transition zone a) Fe_{16}B_4 , b) $\text{Fe}_{15}\text{MoB}_4$, c) $\text{Fe}_{14}\text{Mo}_2\text{B}_4$ and d) $\text{Fe}_{14}\text{Mo}_4\text{B}_2$.

XRD analysis of hardfacing coatings was given in Figure 3. According to XRD analysis that changing alloying element in the coating composition was affected the phases in the microstructure. In the XRD analysis, α -Fe, FeMo_2B_2 , M_2B type boride, $\text{R}-\text{Fe}_{63}\text{Mo}_{37}$ and trace amounts of Fe_3B and μ - Fe_7Mo_6 phase were detected. Normally, $\text{R}-\text{Fe}_{63}\text{Mo}_{37}$ and Fe_3B phase is a non-equilibrium phase formed under rapid cooling conditions [26]. However, it can be seen in trace amounts in a solidified microstructure under dynamic solidification conditions such as the welding process.

SEM images of hardfacing coatings are given in Figure 4. Fe_{16}B_4 based hardfacing coating composition contains 20 atomic% boron. During solidification, the Fe_2B phase is expected to solidify first as seen Fe-B phase diagram given in Figure 5. As the eutectic temperature drops below the eutectic temperature, which is approximately ~ 1177 $^{\circ}\text{C}$, the liquid phase will solidify eutectically. For this reason, primary Fe_2B phases and eutectic α -Fe+ Fe_2B structure can be found in the coating microstructure. However, since the electrode composition passes very close to the eutectic point, the amount of primary phases is expected to be low. In EDS analysis, α -Fe (point 1) represents Fe_2B with a partially block structure (point 2) and α -Fe+ Fe_2B eutectic structure (point 3). Normally, boron element cannot be detected quantitatively by EDS analysis. However, with EDS analysis, signals can be received from points containing boron. As expected, there were trace amount block-structured Fe_2B phases that solidify primarily and the microstructure largely solidifies as eutectic structure.

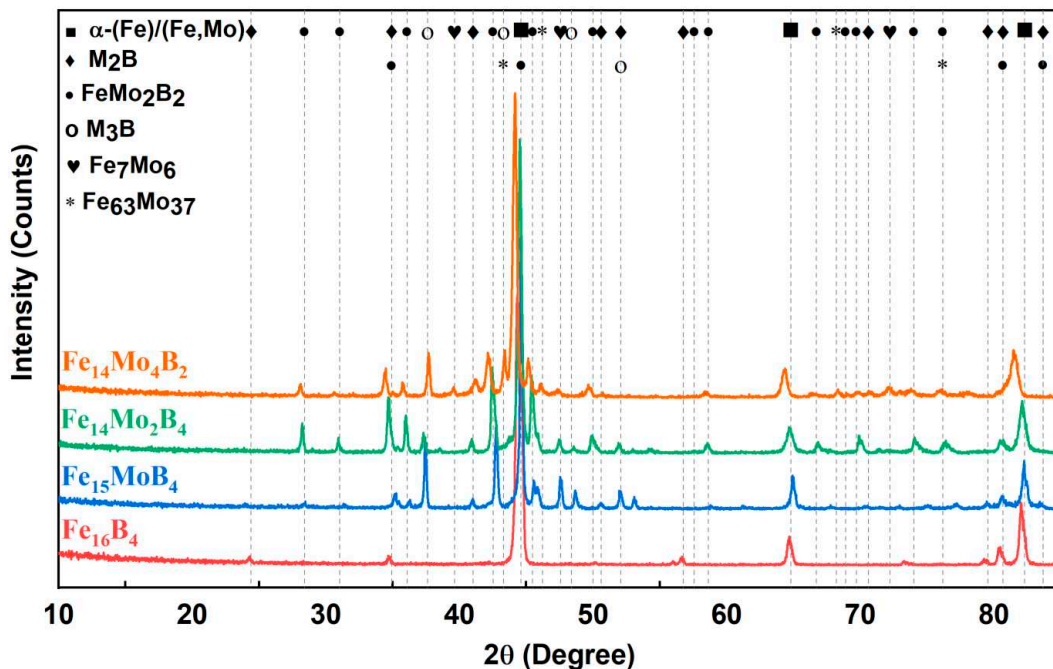


Figure 3. XRD analysis of hardfacing coatings.

It is seen that significant changes occur in the microstructure of the Fe₁₅MoB₄ based coating with the addition of molybdenum in the electrode cover composition. According to EDS and MAB analysis, a molybdenum signal is received from these block-structured phases. It is also understood that these block-structured phases contain boron. It is known that for a fixed boron ratio in the Fe-Mo-B system, increasing the amount of molybdenum shifts the solidification to the hyper-eutectic side [27]. On the other hand, the high melting temperature and thermodynamically stable phase in the Fe₁₅MoB₄ based coating is the FeMo₂B₂ compound [28,29]. For this reason, solidification begins with the formation of FeMo₂B₂ solid crystals and this phase grows with a block structure. After the formation of the FeMo₂B₂ phase, theoretically molybdenum is consumed in the melt, but there is still atomic 15% boron. Solidification continues with the formation of α -Fe, similar to a sub-eutectic composition according to the Fe-B phase diagram. For this reason, there are α -Fe islands around the FeMo₂B₂ phase. When the temperature drops below the eutectic line remaining liquid solidified as α -Fe+Fe₂B eutectic structure and continue to grow. It indicates that the phase detected as M₂B in the XRD analysis is taken from the α -Fe+M₂B structure, which solidifies eutectically around the block structured phases. Although it was assumed that this system solidifies according to the Fe-B phase diagram, the eutectic formed is morphologically different from the eutectic structure formed in the Fe₁₆B₄-based coating. It is known that molybdenum can be dissolved in the Fe₂B phase [30]. Possibly, molybdenum dissolved in the Fe₂B phase causes this phase to solidify as (Fe,Mo)₂B and the morphology of the eutectic structure changes. Similar microstructure has been reported as a reticular eutectic structure in the literature [27]. Also, molybdenum signal was received from EDS region number 2. Although the solubility of molybdenum in α -Fe is quite low under normal conditions, its solubility is ~24% at ~1450 °C. It has been reported that [31,32]. In a process where solidification is dynamic, such as welding, rapid regional or structural cooling might be occurred [24]. For this reason, it was normal for the molybdenum solubility to increase regionally in α -Fe and the dark gray regions are called α -(Fe,Mo). As a result, block-structured FeMo₂B₂, α -(Fe,Mo) and α -Fe+(Fe,Mo)₂B eutectics were expected to form in the final microstructure.

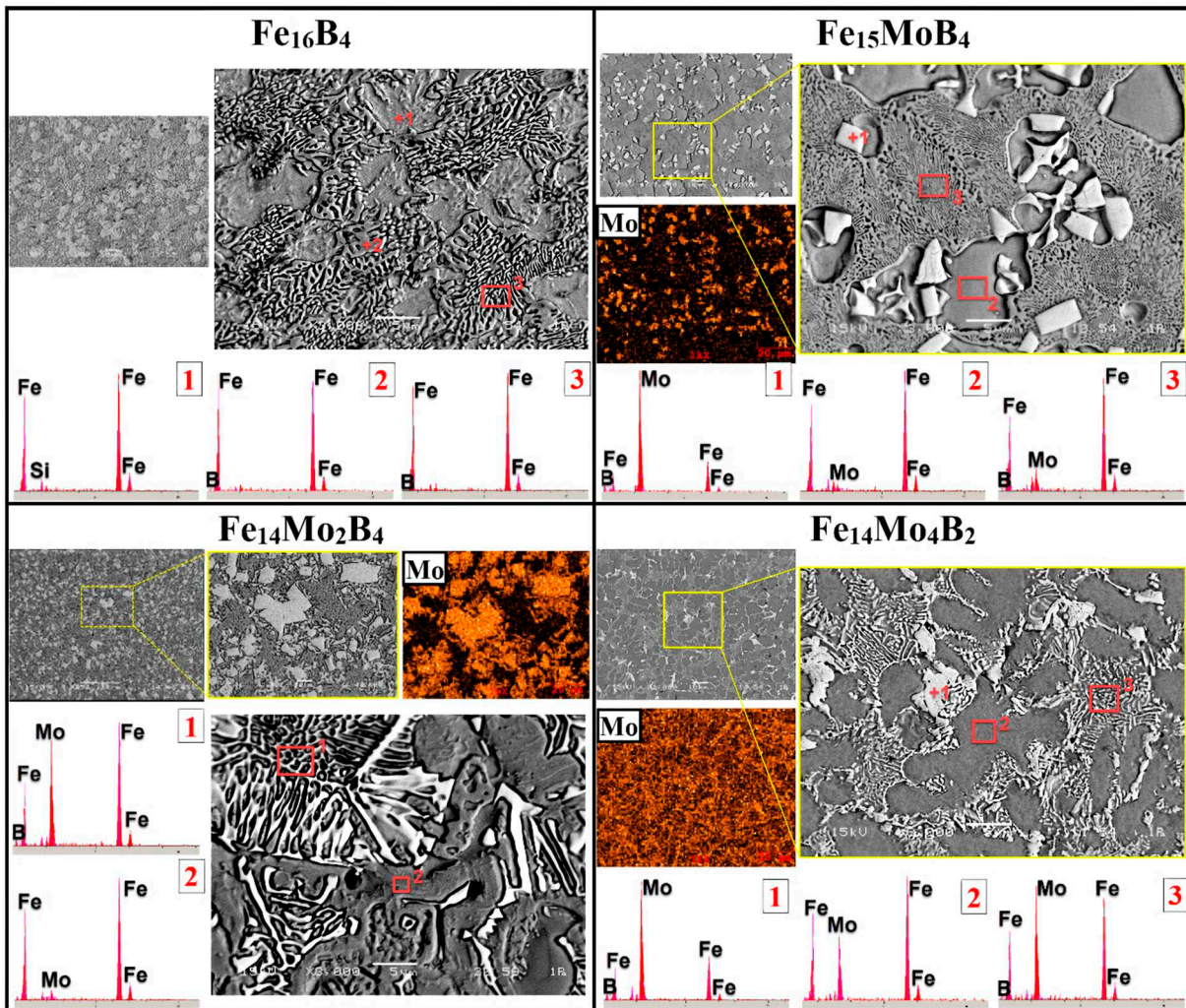


Figure 4. SEM images, EDS and MAP analysis of coatings layer.

There is a significant increase in the ratio of block-structured FeMo_2B_2 phases, in the SEM image of the $\text{Fe}_{15}\text{MoB}_4$ based coating given in Figure 4. The thermodynamic analysis performed with PANDAT software (Figure 5) that similar phases occur in the $\text{Fe}_{14}\text{MoB}_4$ based coating. In XRD analysis, it was determined that the $\text{Fe}_{14}\text{MoB}_4$ based hardfacing coating contained α -Fe, FeMo_2B_2 phase, M_2B type boride and trace amounts of Fe_3B borides in its microstructure. Solidification is expected to begin with the formation of the FeMo_2B_2 phase, similar to the $\text{Fe}_{15}\text{MoB}_4$ -based coating. However, in the microstructure of the $\text{Fe}_{14}\text{MoB}_4$ based coating, it is seen that the block structured phases and the eutectic structure change morphologically. It also has been reported in the literature that the FeMo_2B_2 phase formed in the Fe-Mo-B system can solidify in different forms and the morphology of this phase can change depending on the Mo/B ratio [29]. In similar studies, it has been reported that a eutectic structure consisting of FeMo_2B_2 and Fe_2Mo solid solution can be found around the FeMo_2B_2 phase [30]. However, this eutectic structure solidifies into a morphologically floriform structure. Another phase detected in the XRD analysis, the M_2B type phase, indicates the eutectic solidified Fe_2B phase. As stated in previous studies, Fe_2B can dissolve some molybdenum during solidification and form $(\text{Fe},\text{Mo})_2\text{B}$ phase [30]. The Fe_3B phase detected in trace amounts in the XRD analysis was not visible in the microstructure in a distinguishable. Yin et al. [27] stated that the Fe_3B phase was distributed within the Fe- M_2B eutectic structure. In the final microstructure, consist of FeMo_2B_2 , α -(Fe/Mo)+ FeMo_2B_2 eutectic (floriform structure that solidifies around FeMo_2B_2), α -(Fe/Mo) and α -(Fe/Mo)+(Fe,Mo)₂B (reticular eutectic structure).

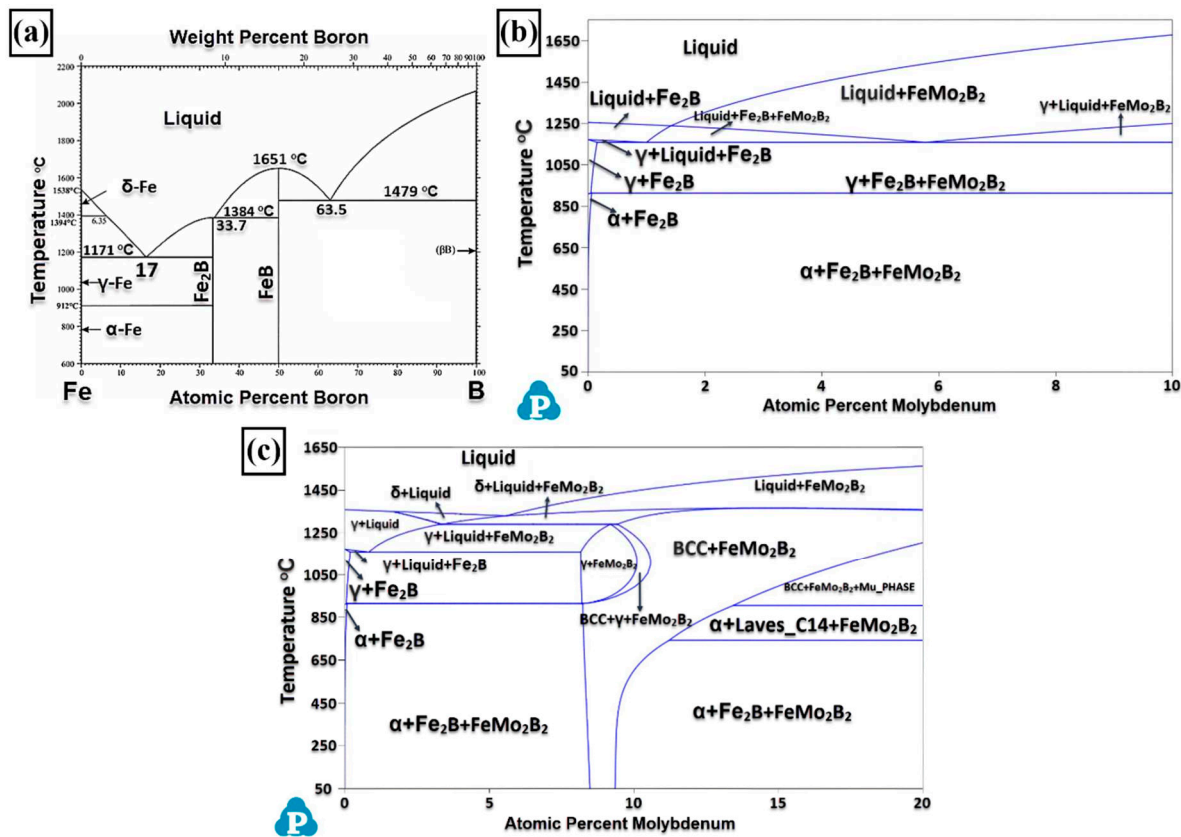


Figure 5. a) Fe-B phase diagram, b and c) equilibrium phase diagram of Fe-Mo-B system.

A structure consisting of light-colored phases, eutectic-like structures with the same contrast as these phases, and a matrix phase can be seen in the SEM image of Fe₁₄Mo₄B₂ based coating. According to the thermodynamic analysis performed with Pandat software, α-Fe, FeMo₂B₂ and phase were expected to be present in the microstructure under stable solidification conditions. However, in XRD analysis, in addition to α-Fe and FeMo₂B₂ phases, μ-Fe₇Mo₆ and R-Fe₆₃Mo₃₇ phases were detected. According to the Fe-Mo phase diagram, the R-Fe₆₃Mo₃₇ phase is an unstable phase below 1200 °C and indicates solidification at a high cooling rate [17]. Molybdenum signal was detected from white island-shaped phases in the EDS analysis. The first phase expected to form under balanced conditions was the FeMo₂B₂ phase. However, the surface of the island-shaped phase shown at EDS point number 1 has a faceted structure, unlike the FeMo₂B₂ phase. Possibly, this phase is the R-Fe₆₃Mo₃₇ phase, which solidifies out of equilibrium, as stated in the literature [17]. The μ-Fe₇Mo₆ phase, which was detected in trace amounts in the XRD analysis, could not be clearly detected in the microstructure. Previous studies also show that this phase is not clearly distinguishable [17,33]. Eutectic regions indicate the FeMo₂B₂ phase detected in XRD analysis. The amount of molybdenum affects not only the morphological properties of FeMo₂B₂ phases but also the morphology of the eutectic structure (α-(Fe,Mo)+FeMo₂B₂). For this reason, increasing the amount of molybdenum and decreasing the boron rate affects the distance between the lamellar in the eutectic structure in the Fe₁₄Mo₄B₂ based coating.

3.2. Hardness and Wear Tests

Figure 6 shows the macro hardness test results of hardfacing coatings. In the coatings carried out on AISI 1020 steel substrate, the lowest and highest hardness change in the substrate material hardness was measured as 58 % in the Fe₁₆B₄-based coating and 73 % in the Fe₁₄Mo₂B₄-based coating, respectively. Additionally, it was observed that an increase in macrohardness as the amount of molybdenum added to the Fe-B based hardfacing electrode composition increases. With 5 % molybdenum added to the electrode cover composition, an increase in hardness of 22.8 % was observed, and with the addition of 10 % molybdenum, an increase in HRC hardness of 30.48% was

observed compared to the Fe₁₆B₄ based coating. On the other hand, the macro hardness value of Fe₁₄Mo₂B₄ based hardfacing coating was measured as 56.5 HRC, while the hardness value of Fe₁₄Mo₄B₂ based hardfacing coating was measured as 49.9 HRC. In other words, the hardness value of Fe₁₄Mo₂B₄ based hardfacing was approximately ~13 % higher than that of Fe₁₄Mo₄B₂ based hardfacing. This shows that although the hardness increases with molybdenum for Fe-Mo-B based coatings, the amount of boron in the coating composition has a significant effect on the increase in hardness. In addition, the top values of hardness were related to the phases in the microstructure and especially the FeMo₂B₂ phase plays an important role in increasing the hardness.

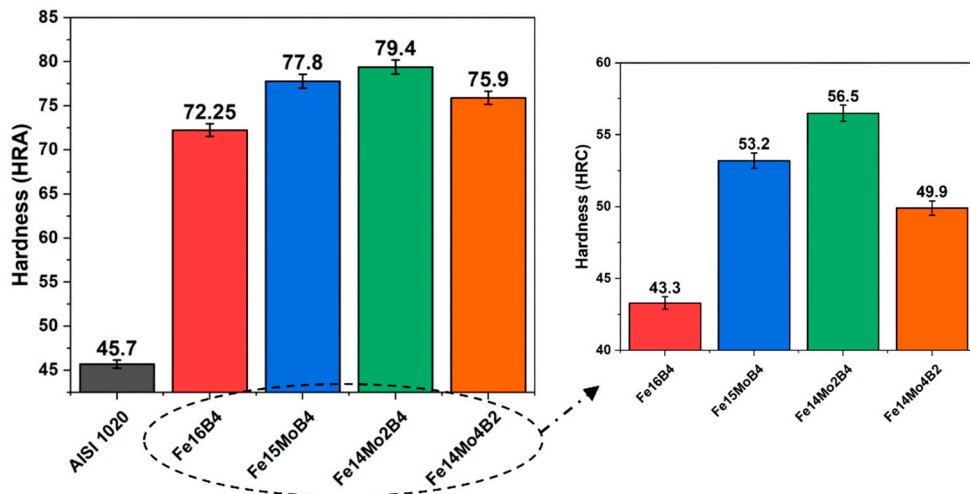


Figure 6. Macro hardness results of hardfacing coatings.

In the study, the lowest microhardness value was measured from the substrate material as seen Table 3. Among the coated samples, the lowest matrix phase hardness was measured in Fe₁₆B₄ based hardfacing coating. The matrix phase hardness of the Fe₁₆B₄ based coating gives almost the same results as the substrate material. The solubility of boron, an interstitial element, in the α -Fe matrix was quite low. For this reason, the boron in the composition was found in Fe₂B or the eutectic phase formed by this phase. With the addition of atomic 5 % molybdenum into the alloy, there was a significant increase in the hardness of the matrix phase. Additionally, it was observed that this increase was not only in the matrix phase but also in the eutectic structure. Due to the nature of the welding process, molybdenum may dissolve to some extent in the matrix phase and the Fe₂B phase. This situation causes an increase in hardness in the matrix phase as a result of solid solution hardening [34]. Similarly, molybdenum dissolved in the Fe₂B phase causes the hardness of this phase to increase. Although the hardness of the other phases was similar, trace changes were observed depending on the composition, especially in the matrix phase. On the other hand, the matrix hardness of the Fe₁₄Mo₄B₂ based coating was less than that of other coatings containing molybdenum. The hardness of the R-Fe₆₃Mo₃₇ phase in the microstructure of the same coating was also measured to be lower than the boron-containing phases. As can be seen from previous studies, changes in both microstructural and atomic dimensions change the hardness of the coating [35,36]. The difference in the matrix phase between the compositions might cause distortion in the lattice, causing the hardness to be slightly different. Microstructurally, each phase prevents dislocation movement, but the physical properties of the phase determine the limit values of plastic deformation. As stated in the literature, boron-containing phases play a decisive role on the hardness of the coating [37]. The hardness values measured from the phases in the microstructure have an effect on the macro hardness. Although the hardness values measured in the study depend on the composition and production method for Fe-Mo-B based alloys, they appear to be compatible with various studies [38–40].

Table 3. Micro hardness results of hardfacing coatings.

Sample	Matrix (HV _{0.01})	Eutectic (α- Fe-M ₂ B) (HV _{0.01})	Eutectic (α- Fe-FeM ₂ B ₂) (HV _{0.01})	FeM ₂ B ₂ (HV _{0.01})	R- (Fe ₆₃ Mo ₃₇) (HV _{0.01})
AISI 1020	143-147	-	-	-	-
Fe ₁₆ B ₄	173-180	478-542	-	-	-
Fe ₁₅ MoB ₄	424-542	996-1200	-	1953-2973	-
Fe ₁₄ Mo ₂ B ₄	459-573	1053-1242	642-956	1970-3228	-
Fe ₁₄ Mo ₄ B ₂	368-379	-	520-754	-	718-840

Figure 7 shows the wear rate graph of hardfacing coatings depending on load and distance. According to the graph, it is understood that the wear rate increases with both increasing distance and increasing load. In the study, the highest wear rate was measured from the substrate material. Among the coated samples, the highest wear rate was measured in Fe₁₆B₄ and the lowest wear rate in Fe₁₄Mo₂B₄ based coating. Wear rates exhibit a similar behavior to the hardness results. As Archard stated [41], the wear rate varies inversely with the hardness. The basic philosophy of hardfacing coatings is to cover the surface with a harder layer than the substrate material. As mentioned above, each hard phase in the microstructure of this hard layer formed on the substrate surface changes the effect of the coating on wear. In addition, not only the hardness of these phases, but also their compatibility with the surface, morphology, etc. properties also affect the wear behavior of the coating. In this study, the hard eutectic α-Fe+Fe₂B structure, which forms the microstructure of the Fe₁₆B₄-based coating, increases the wear resistance of the substrate material. The high hardness FeM₂B₂ phase formed in the microstructure with the addition of molybdenum and the different morphologies of this phase cause further increase in wear resistance. On the other hand, although the wear resistance increases with increasing molybdenum amount, the wear resistance of the Fe₁₄Mo₂B₄ based coating was measured to be higher at all loads and distances than the wear resistance of the Fe₁₄Mo₄B₂ based coating. Boron is a critical element in the formation of hard phases, and the volumetric fraction of the phases formed by boron affects the wear resistance of the coating. In addition, although boron provides the formation of the hard phase, the matrix phase is critical in terms of both hardness and wear resistance. The fact that molybdenum is soluble in the matrix phase and increases its hardness has an effect on wear. Likewise, both the hardness and wear resistance of the Fe₁₆B₄-based coating, where the matrix phase is soft, were measured to be lower than the Fe₁₄Mo₄B₂-based coating.

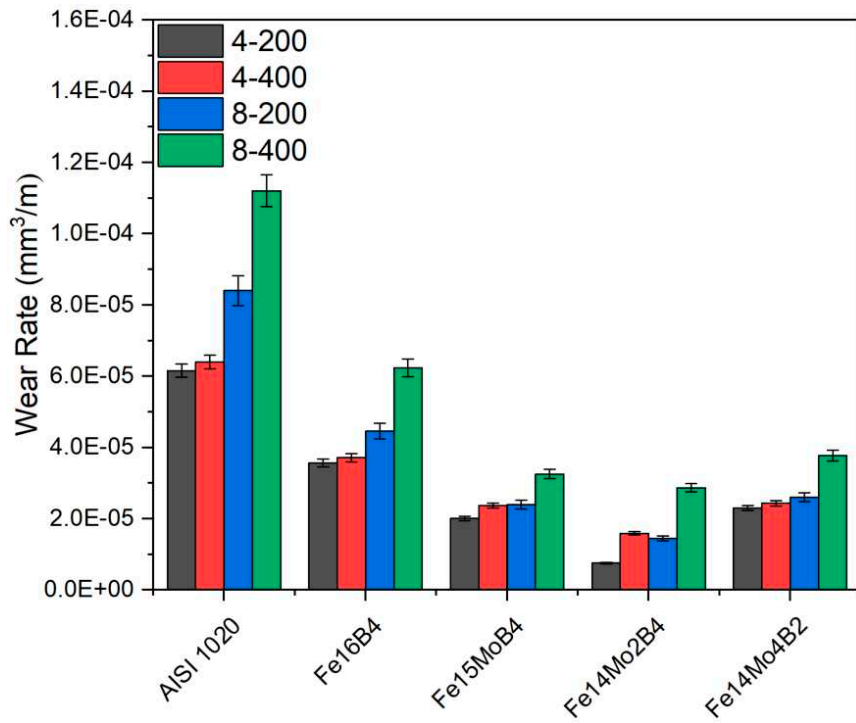


Figure 7. Wear rate of samples.

Figure 8 shows the friction coefficient graphs obtained after the wear test at different loads and distances applied to hardfacing coatings. Friction coefficient values vary between ~ 0.4 - 0.8μ . According to the friction coefficient data of the coated samples, it can be said that the highest friction coefficient value was obtained in Fe₁₆B₄-based hardfacing and the lowest friction coefficient values were obtained in Fe₁₄Mo₄B₂-based hardfacing. The overall friction coefficient is closely related to the surface profile and phases in the microstructure [42–44]. In composite materials such as hardfacing, each phase has a different effect on wear. On the other hand, the hardness, morphology, volumetric ratio and distribution of these phases are other parameters that affect the friction coefficient. The friction coefficients given in Figure 8 act independently of the surface hardness. However, it can be said that the smoothest surface among the samples is on the Fe₁₄Mo₄B₂ based hardfacing coating after the substrate material. On the other hand, the composite structure seen in the microstructures of other coatings is likely to create resistance during sliding. These composite structures might cause an increase in the coefficient of friction. Similar studies in the literature have stated that the coefficient of friction increases with the increase in the amount of hard phase in the metal matrix composite [45]. In the study, no correlation was found in the change of friction coefficient according to load and distance.

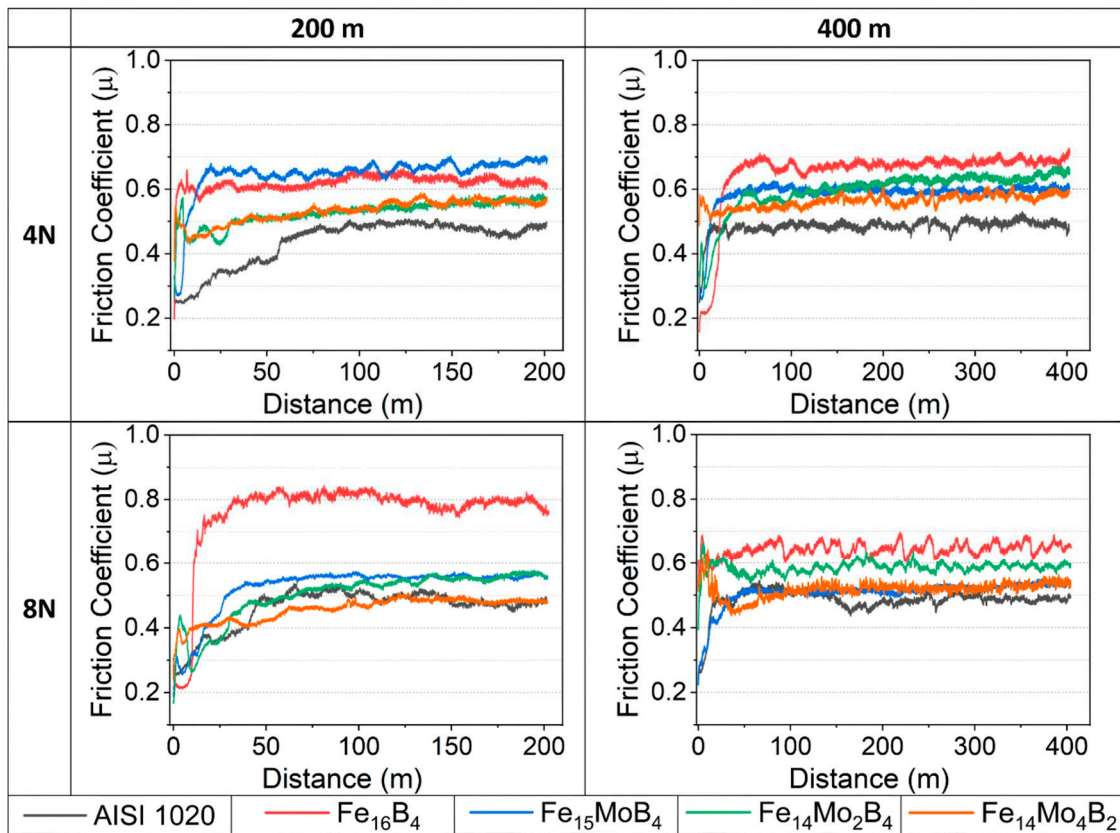


Figure 8. Friction coefficient graph of hardfacing coatings.

In the EDS analysis of the substrate material shown in Figure 9, an intense amount of oxygen signal was received from the dark areas. The formation of a FeO-based oxide layer during wear on the carbon steel surface has been reported in similar studies [46]. On the other hand, the microstructure of the substrate material was not containing factors such as grain boundaries, secondary phases and eutectic structure that would create resistance during wear compared to coated samples. For this reason, friction occurs on a smoother surface. In the friction coefficient graph given in Figure 8, it reached the steady state wear phase after a short running-in period. The homogeneous oxide layer formed on the surface might acted as a solid lubricant, causing the friction coefficient to be relatively lower than other samples. On the other hand, it is seen that this oxide layer forms debris at some points. Local adhesions may occur as a result of micro-weld in softer and easily oxidized substrate material. Increasing heat during friction and the change in surface topography due to the oxide layer formed may also cause fluctuations in the friction coefficient [47]. On the other hand, oxide-based debris formed as a result of the delamination of the oxide layer was seen in the SEM image of the substrate material. It was understood that wear was dominated by oxidative and adhesive wear mechanism. The worn surface appearance of the hardfacing coated samples shown in Figure 9 shows that the oxidized parts remained more localized compared to the substrate material.

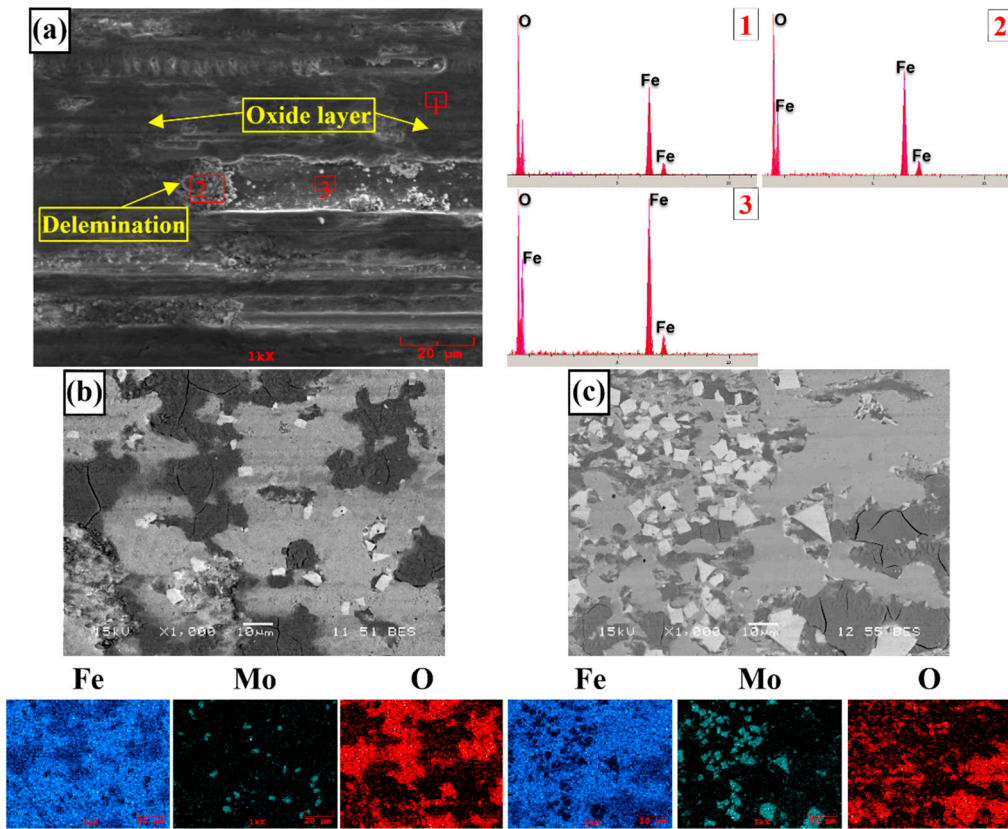


Figure 9. wear surfaces of a) AISI 1020 steel substrate b) $\text{Fe}_{15}\text{MoB}_4$ based coating and c) $\text{Fe}_{14}\text{Mo}_2\text{B}_4$ based coating.

As a result of the SEM analysis performed on the coated samples, different mechanisms played an active role during wear. It can be seen that debris and delaminations were formed on the surface of the Fe_{16}B_4 -based hardfacing coating shown in Figure 10-a after wear. Debris might be occurred due to the sawing effect created by the eutectic phase during friction. It was also observed that delamination occurs in the soft (matrix) phase during friction in the eutectic structure. This indicates that it might be pulled out due to adhesion formed in the soft matrix phase with increasing heat in the later stages of friction. With the addition of molybdenum, the delamination of hard phases formed in the microstructure decreased by reducing the oxide detachment on the surface. However, the abrasive wear increases with increasing hard phase fraction and micro abrasive lines appear on the surface. One of the basic mechanisms expected to develop during the wear of hardfacing coatings is microabrasive wear, which was expected to occur due to three-body wear mechanism. As a result of the micro-abrasive wear mechanism, small pieces pulled out from the friction surfaces were plastered on the surface, causing wear called smeared [48–50]. The SEM image and MAP analysis shown in Figure 9 indicate this situation, where cracks occur directly in oxidized areas. Similarly, the cracks formed in Figure 10-b and c indicate removal from the surface after smearing. On the other hand, block-structured phases formed by the addition of molybdenum caused a large hardness difference between the matrix and the particle. The difference in hardness between the matrix and the hard phase might be caused fatigue in the matrix phase. Fatigue occurring during wear might cause fatigue cracks and subsequent ruptures after a while. In addition, in the SEM image of the $\text{Fe}_{15}\text{MoB}_2$ based coating given in Figure. As a result, hard phases such as M_2B and FeMo_2B_2 play an active role during friction. These hard phases and eutectic structures were in direct contact with the abrasive. For this reason, the increasing amount of block-structured or eutectic hard phase acts in the direction of increasing wear resistance. Similar results have been reported in previous studies [19]. In the study, it was determined that micro abrasive, adhesive and oxidative wear were dominant wear mechanism.

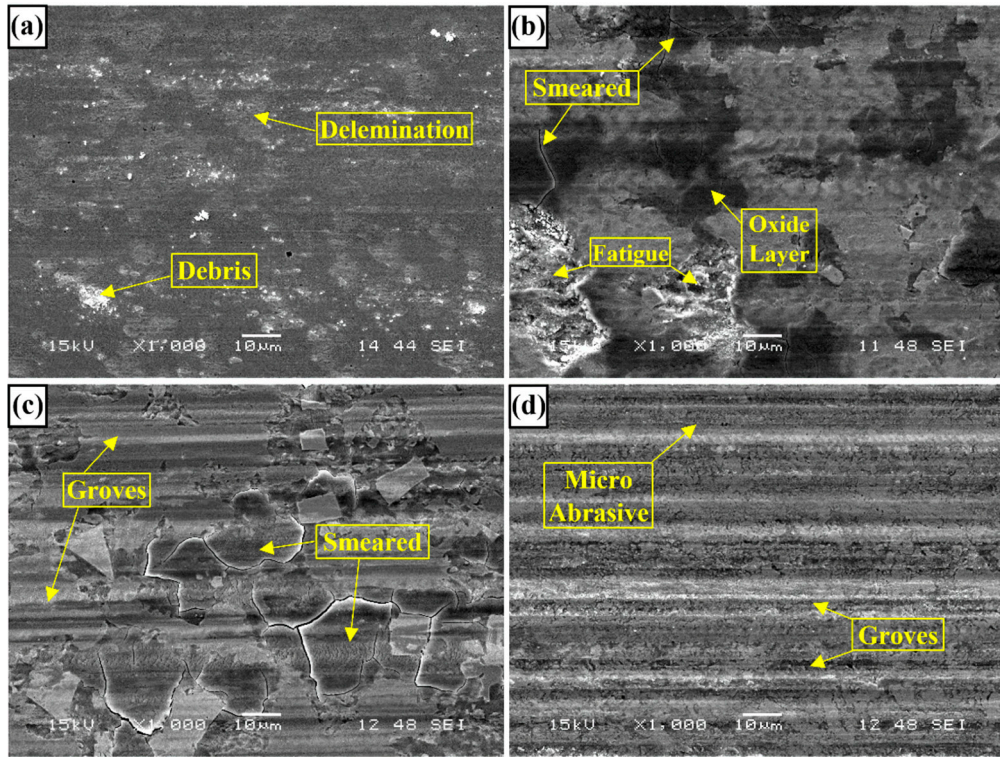


Figure 10. Wear surface of hardfacing coatings a) Fe₁₆B₄, b)Fe₁₅MoB₄, c) Fe₁₄Mo₂B₄ and d) Fe₁₄Mo₄B₂.

3.3. Corrosion Behavior

OCP curves were given in Figure 11-a. The OCP curves become stable in a short time. As stated in the literature, when the open circuit potential reaches equilibrium, it indicates that the film formation and dissolution on the surface are in balance [51]. In all OCP curves, there was first a slight movement towards the anodic side, and then the curves became stable. The OCP value of the substrate material was measured to be slightly more positive than the coated samples. This might be due to the oxide layer that forms more easily on the surface of the substrate material. According to the OCP test, anodic corrosion tendency decreased with increasing molybdenum amount in the coating composition. The OCP value of the Fe₁₆B₄-based coating was measured to be similar to molybdenum-containing coatings.

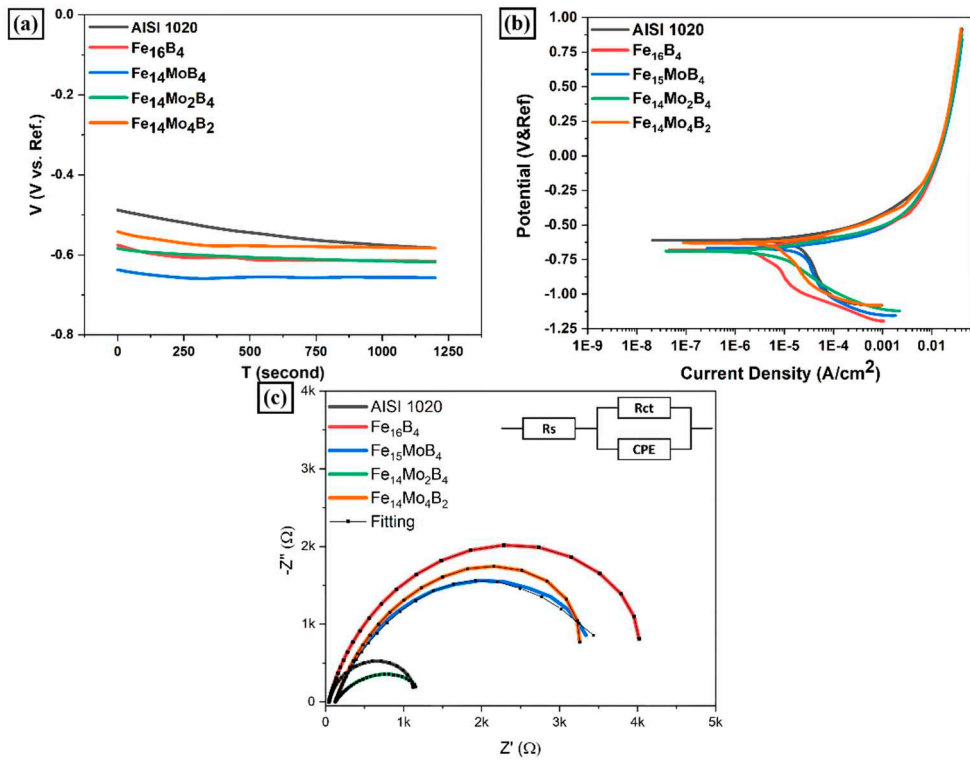


Figure 11. a) OCP diagram and b) Tafel curves of coating layers c)EIS diagram.

Tafel curves obtained from samples subjected to electrochemical corrosion test in 0.5 M NaCl solution were given in Figure 11-b. The corrosion potential obtained from these curves gives information about the direction of corrosion [19,52]. According to the curves, there was no big difference in corrosion potentials. However, the most noble sample in terms of corrosion potential is the AISI 1020 steel substrate. In other words, it was the sample substrate material with the least corrosion tendency according to its corrosion potential. According to the corrosion parameters given in Table 4, it is seen that the addition of molybdenum to the molybdenum Fe-B based coating composition does not cause a linear change on the corrosion potential. Among the coated samples, the noblest corrosion potential was measured in the Fe₁₄Mo₄B₂ based coating. On the other hand, current density, which is a critical parameter in the kinetic interpretation of corrosion, is directly related to the rate of corrosion. According to corrosion current density values, the lowest current density was measured in Fe₁₆B₄ based coating. Many researchers have reported that Fe-B alloys near the eutectic point have very good corrosion resistance [53–56]. There was a decrease in the current density values with the addition of molybdenum into the Fe₁₆B₄ based coating. In other words, the corrosion resistance of the coating has increased.

Table 4. Tafel parameters of hardfacing coatings.

Sample	E _{cor} mV	I _{cor} μ A/cm ²	Cr (mpy)
AISI 1020	-609.315	28.331	16.291
Fe ₁₆ B ₄	-683.455	2.078	1.544
Fe ₁₅ MoB ₄	-669.678	15.287	11.245
FeMo ₂ B ₄	-688.666	6.601	4.808
FeMo ₄ B ₂	-632.627	5.650	3.603

Another method used to understand corrosion in kinetic terms is the EIS method. The similarity of the EIS curves seen in Figure 11-c indicates that similar corrosion mechanisms have developed in the coating layers. On the other hand, the diameter of the capacitive loop varies in direct proportion

to the corrosion resistance. In other words, the corrosion resistance of the coating with a large capacitive loop diameter is high [57,58]. EIS test parameters obtained by equivalent circuit modeling are given in Table 5. According to the model, R_s is a measure of solution resistance and R_{ct} is a measure of polarization resistance. A higher R_{ct} value indicates higher corrosion resistance. The fact that both the capacitive loop diameter and the R_{ct} value are large indicates that the corrosion resistance of the $Fe_{16}B_4$ based coating is higher. This can be associated with the microstructure of the $Fe_{16}B_4$ -based coating. Factors such as phases and grain boundaries within the microstructure increase the polarization resistance [59]. R_{ct} resistance increases especially in $Fe_{16}B_4$ based coatings that contain a high fraction of eutectic structure. According to EIS data, AISI 1020 steel substrate, which does not contain grain boundaries in the microstructure, has low corrosion resistance. Although the microstructure of the $Fe_{14}Mo_2B_4$ based coating is complex, the R_{ct} value was low. This may be related to the morphology and composition of the eutectic structure.

Table 5. EIS test parameters.

Sample	R_s (Ω)	$CPE-1$ ($\mu F.cm^{-2}$)	R_{ct-1} ($k\Omega$)
AISI 1020	42.78	2.2e-4	1.29
$Fe_{16}B_4$	40.41	2.29e-4	4.87
$Fe_{15}MoB_4$	126.3	1.08e-4	4.25
$Fe_{14}Mo_2B_4$	134.4	2.43e-4	1.4
$Fe_{14}Mo_4B_2$	129	1.11e-4	4.38

In the post-corrosion SEM image of the substrate material shown in Figure 12, it is seen that a like cotton layer is covered on the surface. In the EDS analysis carried out in this region, intense signals belonging to Fe and Cl elements were received. This indicates that the iron on the surface is dissolved as a result of the anodic reaction and ferrous salts are formed on the surface.

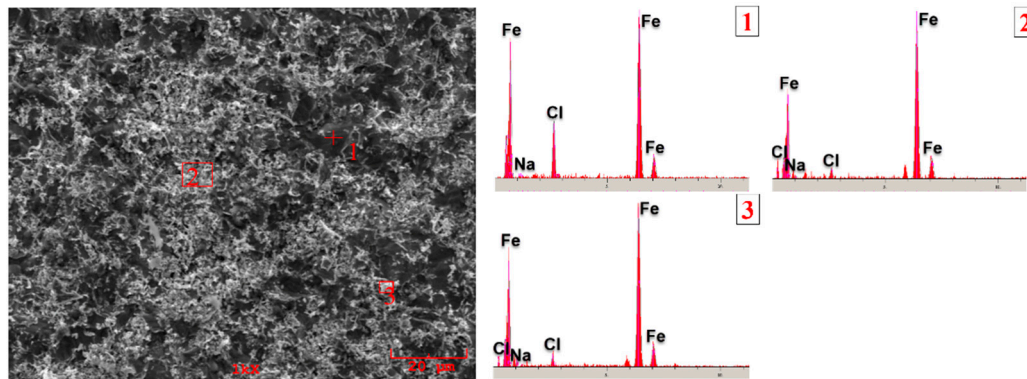


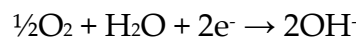
Figure 12. Corroded surface of AISI 1020 steel substrate.

The reaction of anodic dissolution occurring on the substrate surface is the oxidation reaction of α -Fe and is expected to occur according to the reaction given below. In the SEM image, it is understood that this reaction develops homogeneously on the surface. This type of homogeneous corrosion is a less dangerous corrosion mechanism and generally the homogeneous oxide layer formed on the surface polarizes the surface. However, the breakdown of this layer accelerates corrosion.

Anodic reaction [60,61]:



Cathodic Reaction:



direct oxygen reduction of cathodic reaction

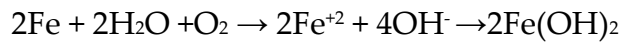


Figure 13 shows SEM images of hardfacing coatings after corrosion. In the images, there was no corrosion damage in the parts formed by FeMo_2B_2 , $\text{R-Fe}_{63}\text{Mo}_{37}$ and these phases within this eutectic, but there was a significant amount of dissolution in the $\alpha\text{-Fe}/(\text{Fe},\text{Mo})$ regions between the matrix phase and the eutectic phase. This situation indicates the formation of galvanic corrosion caused by the potential difference between the boride phase and $\alpha\text{-Fe}$. Also, this results in selective corrosion of the matrix phase.

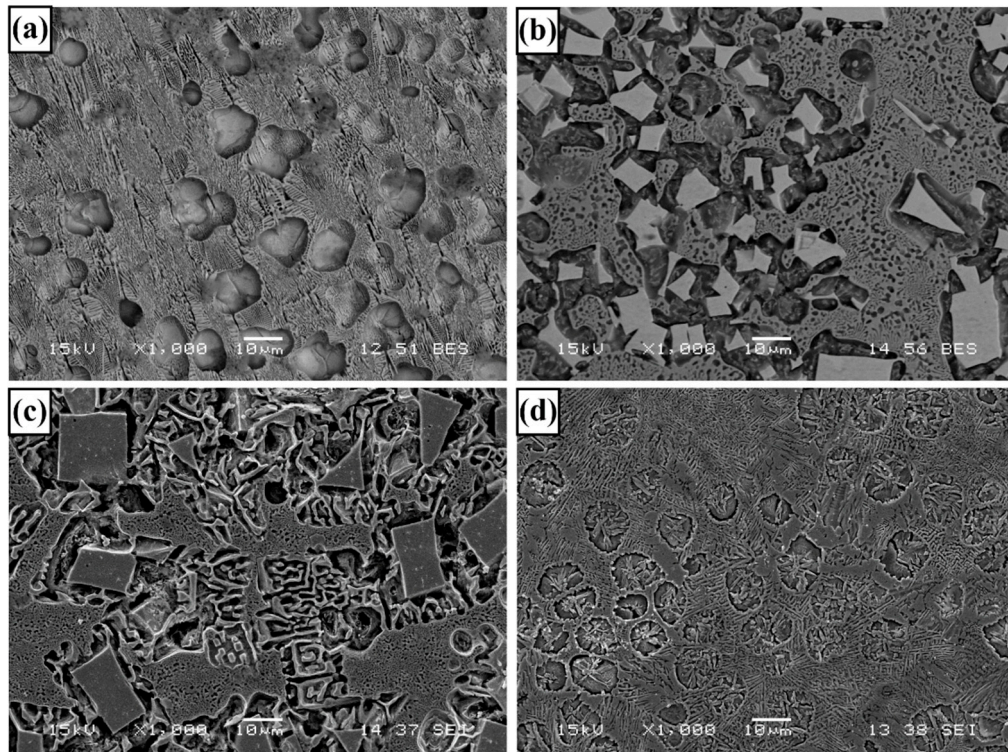


Figure 13. Corroded surface of a) Fe_{16}B_4 , b) $\text{Fe}_{15}\text{MoB}_4$, c) $\text{Fe}_{14}\text{Mo}_2\text{B}_4$ and d) $\text{Fe}_{14}\text{Mo}_4\text{B}_2$ based hardfacing coatings.

In Fe_{16}B_4 based coating, the matrix phase consists of $\alpha\text{-Fe}$ and dissolution can be occurred according to the reactions given above. The molybdenum added to the Fe_{16}B_4 -based coating might have increased the corrosion resistance of the matrix by dissolving it in the matrix phase. Similarly, there was a significant dissolution in the phases around the FeMo_2B_2 phase. As a result of the potential difference between the FeMo_2B_2 phase and the surrounding phases, it may have an accelerating effect on dissolution. Similarly, it has been reported in the literature that the low-molybdenum-containing phase in the region adjacent to the high-molybdenum-containing phase in the eutectic structure will corrode preferentially and cause intergranular corrosion [62]. It was also clearly seen in SEM images. In the SEM image and MAP analysis given in Figure 14, the iron signal received from the eutectic region shows that there was no dissolution in these regions. That is, both M_2B and FeMo_2B_2 phases behave as noble with respect to the matrix phase.

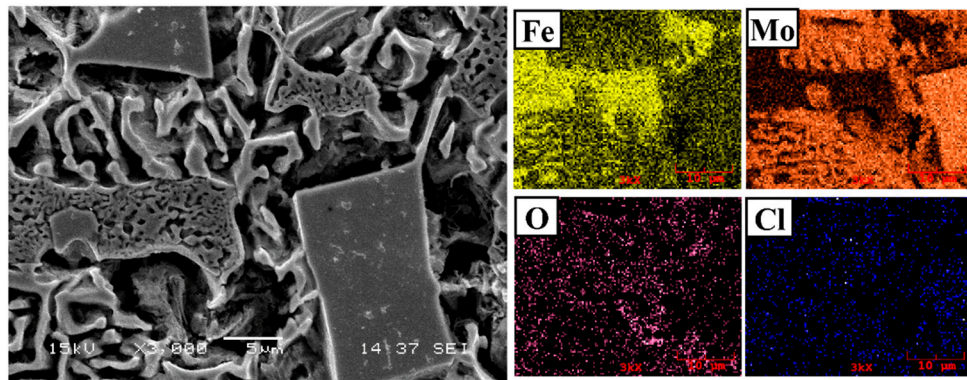


Figure 14. Corroded surface of $\text{Fe}_{14}\text{Mo}_2\text{B}_4$ based coating.

4. Conclusions

In this study, it was aimed to investigate the effect of molybdenum on Fe-B based hardfacing coating and Fe-Mo-B based hardfacing electrodes were produced in different ratios. These produced electrodes were observed microstructurally and hardness, wear and corrosion tests were performed. Additionally, the results were compared with AISI 1020 steel substrate and Fe-B based hardfacing. The findings obtained in the study are as follows;

- It has been determined that changes made in the electrode cover composition change the phases in the microstructure and that even trace changes have a significant morphological effect on some phases. In the study, α -Fe, FeMo_2B_2 , Fe_2B , and $\text{R-Fe}_{63}\text{Mo}_{37}$ phases were detected as major phases, and Fe_3B and Fe_7Mo_6 phases were detected as minor phases. It has also been determined that molybdenum can dissolve in the α -Fe and Fe_2B phase and can affect the morphological and mechanical properties of both these phases and the eutectic structures formed by these phases.
- Neither molybdenum nor boron could provide the effect of both on the hardness and wear resistance of the coating. In addition, this effect reaches its maximum level for mixtures made in certain proportions. For this reason, optimizing the compositions in hardfacing coating works was critical. In the study, the highest macro hardness value was obtained in the $\text{Fe}_{14}\text{Mo}_2\text{B}_4$ based coating as 56.4 HRC. It was observed that the hardness of this coating was ~73 % higher than the substrate material and ~30.5 % higher than the Fe_{16}B_4 based coating. According to microhardness measurements, although the hardness of the phases in the microstructure varies over a wide range, the highest phase hardness was measured as 3228 HV in the FeMo_2B_2 phase. In the study, the highest wear resistance was obtained in the $\text{Fe}_{14}\text{Mo}_2\text{B}_4$ based coating. According to the wear rate values, up to ~8.1 times higher wear resistance was obtained in the $\text{Fe}_{14}\text{Mo}_2\text{B}_4$ based coating compared to the AISI 1020 substrate material and up to ~4.7 times higher than the Fe_{16}B_4 based coating.
- According to the corrosion test results, it was observed that there was no significant difference between the corrosion potentials of the substrate material and coated samples. However, a significant difference was detected between the corrosion current density values. The current density of all samples with hardfacing coating is lower than the base material, meaning their corrosion resistance was better. In the study, the lowest current density value was measured as $2.078 \mu\text{A}/\text{cm}^2$ in the Fe_{16}B_4 -based coating and it was found to be ~13.6 times more resistant to corrosion than the substrate material. Although the corrosion resistance of Fe_{16}B_4 -based coating, that is, molybdenum-free, was high, it has been determined that the corrosion resistance increases with increasing molybdenum amount in molybdenum-containing hardfacing coatings.

Funding: The study has been supported by Scientific and Technological Research Council of Türkiye (TÜBİTAK) project number 219M195.

Data Availability Statement: The data cannot be made publicly available upon publication because no suitable repository exists for hosting data in this field of study. The data that support the findings of this study are available upon reasonable request from the authors.

Acknowledgments: The author would like to thank Zonguldak Bülent Ecevit University and Sakarya University, whose laboratory facilities were used to carry out the study.

Orcid iDs: Engin KOCAMAN <https://orcid.org/0000-0001-5617-3064>.

References

1. Zhang K, Zheng Z, Zhang L, Liu Y, Chen S. Method for Dynamic Prediction of Oxygen Demand in Steelmaking Process Based on BOF Technology. *Processes* 2023;11. <https://doi.org/10.3390/pr11082404>.
2. Steel pipe coatings market to hit \$14.0 billion by 2033. *Focus Powder Coatings* 2023;2023:6. <https://doi.org/https://doi.org/10.1016/j.fopow.2023.06.031>.
3. Pelser WA, Marais JH, van Laar JH, Mathews EH. Development and Application of an Integrated Approach to Reduce Costs in Steel Production Planning. *Process Integr Optim Sustain* 2022;6:819–36. <https://doi.org/10.1007/s41660-022-00237-3>.
4. Schubert E, Klassen M, Zerner I, Walz C, Sepold G. Light-weight structures produced by laser beam joining for future applications in automobile and aerospace industry. *J Mater Process Technol* 2001;115:2–8. [https://doi.org/https://doi.org/10.1016/S0924-0136\(01\)00756-7](https://doi.org/https://doi.org/10.1016/S0924-0136(01)00756-7).
5. Dong Q, Chen X, Gao Y, Hu J, Chen X, Xu G. Steel BT - Civil Engineering Materials for Transportation Infrastructure. In: Dong Q, Chen X, Gao Y, Hu J, Chen X, Xu G, editors., Singapore: Springer Nature Singapore; 2023, p. 267–96. https://doi.org/10.1007/978-981-99-1300-8_8.
6. Ren X, Fu H, Xing J, Yi Y. Research on high-temperature dry sliding friction wear behavior of CaTi modified high boron high speed steel. *Tribol Int* 2019;132:165–76. <https://doi.org/https://doi.org/10.1016/j.triboint.2018.12.009>.
7. Qi Y, Luo H, Zheng S, Chen C, Lv Z, Xiong M. Effect of Temperature on the Corrosion Behavior of Carbon Steel in Hydrogen Sulphide Environments. *Int J Electrochem Sci* 2014;9:2101–12. [https://doi.org/https://doi.org/10.1016/S1452-3981\(23\)07914-2](https://doi.org/https://doi.org/10.1016/S1452-3981(23)07914-2).
8. Liu DS, Liu RP, Wei YH, Pan P. Properties of cobalt based hardfacing deposits with various carbon contents. *Surf Eng* 2013;29:627–32. <https://doi.org/10.1179/1743294413Y.0000000162>.
9. Hutchings I, Shipway P. 7 - Surface engineering. In: Hutchings I, Shipway PBT-T (Second E, editors., Butterworth-Heinemann; 2017, p. 237–81. <https://doi.org/https://doi.org/10.1016/B978-0-08-100910-9.00007-6>.
10. Vasilescu M, Dobrescu M. Hardfacing Corrosion and Wear Resistant Alloys. *Mater. Res. Appl.*, vol. 1114, Trans Tech Publications Ltd; 2015, p. 196–205. <https://doi.org/10.4028/www.scientific.net/AMR.1114.196>.
11. Kocaman E, Kılıç B, Şen S, Şen U. Development of Surface Properties with In Situ TiB₂ Intermetallic-Assisted Coating by Fe(18-X)Ti₂B_X (x = 3,4,5)-Based Electrodes. *Arab J Sci Eng* 2021. <https://doi.org/10.1007/s13369-021-06304-0>.
12. Trembach B. Comparative studies of the three-body abrasion wear resistance of hardfacing Fe-Cr-C-B-Ti alloy. *IOP Conf Ser Mater Sci Eng* 2023;1277:012016. <https://doi.org/10.1088/1757-899x/1277/1/012016>.
13. Ardigo-Besnard MR, Tellier A, Besnard A, Chateau-Cornu J-P. Effect of the microstructure on the tribological properties of HIPed and PTA-welded Fe-based hardfacing alloy. *Surf Coatings Technol* 2021;425:127691. <https://doi.org/https://doi.org/10.1016/j.surfcoat.2021.127691>.
14. Kılıç B, Kocaman E, Şen S, Şen U. Effect of vanadium content on the microstructure and wear behavior of Fe(13-x)VxB₇ (x = 0–5) based hard surface alloy layers. *Mater Charact* 2021;179:111324. <https://doi.org/https://doi.org/10.1016/j.matchar.2021.111324>.
15. Chen C, Wang J, Ge Y, Zhuang M, Ma Z. Microstructure and Wear Resistance of High-Chromium Cast Iron with Multicomponent Carbide Coating via Laser Cladding. *Coatings* 2023;13. <https://doi.org/10.3390/coatings13081474>.
16. Durmuş H, ÇÖMEZ N, Gül C, Yuddaşkal M, Uzun RO. Ferromolibden ve ferrobor takviyeli lazer kaplamaların aşınma karakteristiği ve mikroyapısı. *DÜMF Mühendislik Derg* 2019;10:1009–17. <https://doi.org/10.24012/dumf.511737>.
17. Deng X, Zhang G, Wang T, Ren S, Bai Z, Cao Q. Investigations on microstructure and wear resistance of Fe-Mo alloy coating fabricated by plasma transferred arc cladding. *Surf Coatings Technol* 2018;350:480–7. <https://doi.org/https://doi.org/10.1016/j.surfcoat.2018.07.040>.
18. Dilawary SAA, Motallebzadeh A, Paksoy HA, Akhter R, Atar E, Cimenoglu H. LSM of Stellite 12 + 10wt % Mo hardfacing alloy for enhancement in wear resistance, Mons: XXXI International Conference on Surface Modification Technologies (SMT31); 2016.
19. Li Q, Wang Q, Zhang L, Chen DX, Jin H, Li JD, et al. Microstructure, wear and electrochemical behaviors of laser cladding Fe-based coatings with various molybdenum contents. *Mater Res Express* 2022;9. <https://doi.org/10.1088/2053-1591/ac4e3d>.
20. Jiang R, Sen, Wang YT, Hu L, Xu G, Liu Z, De. Effect of Mo Content on the Corrosion Resistance of Fe-Based Amorphous Composite Coating. *Mater Sci Forum* 2016;849:636–41. <https://doi.org/10.4028/www.scientific.net/MSF.849.636>.

21. Hazza MI, El-Dahshan ME. The effect of molybdenum on the corrosion behaviour of some steel alloys. *Desalination* 1994;95:199–209. [https://doi.org/https://doi.org/10.1016/0011-9164\(94\)00014-X](https://doi.org/10.1016/0011-9164(94)00014-X).
22. B.ROCKEL M. The Effect of Molybdenum on the Corrosion Behavior of Iron-Chromium Alloys. *Corrosion* 2013;29:393–6. <https://doi.org/10.5006/0010-9312-29.10.393>.
23. Kocaman E, Kılınç B, Şen S, Şen U. In-situ TiB₂ and Fe₂Ti intermetallic assisted hard coatings by Fe-Ti-B based hardfacing electrodes. *J Alloys Compd* 2022;900. <https://doi.org/10.1016/j.jallcom.2021.163478>.
24. Kocaman E, Kılınç B, Şen S, Şen U. Effect of chromium content on Fe(18-x)Cr_xB₂(X=3,4,5) hardfacing electrode on microstructure, abrasion and corrosion behavior. *J Fac Eng Archit Gazi Univ* 2020;36:177–90. <https://doi.org/10.17341/gazimfd.689230>.
25. Duraisamy R, Kumar SM, Kannan AR, Shanmugam NS, Sankaranarayanasamy K, Ramesh MR. Tribological performance of wire arc additive manufactured 347 austenitic stainless steel under unlubricated conditions at elevated temperatures. *J Manuf Process* 2020;56:306–21. <https://doi.org/10.1016/j.jmapro.2020.04.073>.
26. Sunbul SE, Akyol S, Onal S, Ozturk S, Sozeri H, Icin K. Effect of Co, Cu, and Mo alloying metals on electrochemical and magnetic properties of Fe-B alloy. *J Alloys Compd* 2023;947:169652. <https://doi.org/https://doi.org/10.1016/j.jallcom.2023.169652>.
27. Ouyang X, Chen G, Yin F, Liu Y, Zhao M. Effect of Molybdenum on the Microstructures of As-Cast Fe-B Alloys and Their Corrosion Resistance in Molten Zinc. *Corrosion* 2017;73:942–52. <https://doi.org/10.5006/2280>.
28. Beardsley BM, Sebright JL. Structurally Integrated Coatings for Wear and Corrosion. 2018.
29. Wang HQ, Sun JS, Li CN, Geng SN, Sun HG, Wang GL. Microstructure and mechanical properties of molybdenum–iron–boron–chromium cladding using argon arc welding. *Mater Sci Technol (United Kingdom)* 2016;32:1694–701. <https://doi.org/10.1080/02670836.2016.1140926>.
30. Sarasola M, Gómez-Acebo T, Castro F. Microstructural development during liquid phase sintering of Fe and Fe–Mo alloys containing elemental boron additions. *Powder Metall* 2005;48:59–67. <https://doi.org/10.1179/003258905X37558>.
31. Guillermet AF. The Fe–Mo (Iron–Molybdenum) system. *Bull Alloy Phase Diagrams* 1982;3:359–67. <https://doi.org/10.1007/BF02869315>.
32. Cho I-S, Savelyev KD, Golod VM. Development of thermophysical calculator for stainless steel casting alloys by using CALPHAD approach. *China Foundry* 2017;14:353–8. <https://doi.org/10.1007/s41230-017-7144-5>.
33. Utkin S V., Bondar AA, Kublii VZ, Kapitanchuk LM, Tikhonova IB. Solidus Surface of the Mo–Fe–B System. *Powder Metall Met Ceram* 2020;59:89–105. <https://doi.org/10.1007/s11106-020-00141-w>.
34. Chen K, Yang X, Li W, Xia G, Wang S, Wang K. Study on the wear and corrosion resistance of Fe–Mo coatings on 65Mn steel ploughshares by laser cladding. *Appl Phys A* 2022;128:795. <https://doi.org/10.1007/s00339-022-05869-3>.
35. Huang Z, Xing J, Guo C. Improving fracture toughness and hardness of Fe₂B in high boron white cast iron by chromium addition. *Mater Des* 2010;31:3084–9. <https://doi.org/https://doi.org/10.1016/j.matdes.2010.01.003>.
36. Lentz J, Röttger A, Theisen W. Hardness and modulus of Fe₂B, Fe₃(C,B), and Fe₂₃(C,B)₆ borides and carbaborides in the Fe–C–B system. *Mater Charact* 2018;135:192–202. <https://doi.org/https://doi.org/10.1016/j.matchar.2017.11.012>.
37. Zhang H, Pan Y, Zhang Y, Lian G, Cao Q, Yang J. Sensitivity Analysis for Process Parameters in Mo₂FeB₂ Ternary Boride Coating by Laser Cladding. *Coatings* 2022;12. <https://doi.org/10.3390/coatings12101420>.
38. Azakli Y, Cengiz S, Tarakci M, Gencer Y. Characterisation of boride layer formed on Fe–Mo binary alloys. *Surf Eng* 2016;32:589–95. <https://doi.org/10.1080/02670844.2016.1148322>.
39. Hocaoglu R. Fe–Mo–Ti–B–C esaslı sert dolgu alaşımı örtülü elektrotların üretimi ve özelliklerinin incelenmesi = The production and investigation of the properties of Fe–Mo–Ti–B–C based hardfacing alloy covered electrodes. Sakarya University, 2021.
40. Márquez-Herrera A, Fernandez-Muñoz JL, Zapata-Torres M, Melendez-Lira M, Cruz-Alcantar P. Fe₂B coating on ASTM A-36 steel surfaces and its evaluation of hardness and corrosion resistance. *Surf Coatings Technol* 2014;254:433–9. <https://doi.org/https://doi.org/10.1016/j.surfcoat.2014.07.001>.
41. Archard JF. Contact and Rubbing of Flat Surfaces. *J Appl Phys* 1953;24. <https://doi.org/https://doi.org/10.1063/1.1721448>.
42. Sedláček M, Podgorník B, Vižintin J. Influence of surface preparation on roughness parameters, friction and wear. *Wear* 2009;266:482–7. <https://doi.org/https://doi.org/10.1016/j.wear.2008.04.017>.
43. Buckley DHBT-TS, editor. Chapter 8 Lubrication of Solid Surfaces. *Surf. Eff. Adhes. FrictiON, Wear, Lubr.*, vol. 5, Elsevier; 1981, p. 511–52. [https://doi.org/https://doi.org/10.1016/S0167-8922\(08\)70681-3](https://doi.org/https://doi.org/10.1016/S0167-8922(08)70681-3).
44. Szeri AZ. Tribology. In: Meyers RABT-E of PS and T (Third E, editor., New York: Academic Press; 2003, p. 127–52. <https://doi.org/https://doi.org/10.1016/B0-12-227410-5/00791-2>.

45. Kalel SM, Patil SR. Ceramic Reinforced Metal Matrix Composite (MMC) - Processing. *Int J Adv Res Sci Eng* 2018;7:1047-58.
46. Lee HY. Effect of Changing Sliding Speed on Wear Behavior of Mild Carbon Steel. *Met Mater Int* 2020;26:1749-56. <https://doi.org/10.1007/s12540-019-00417-w>.
47. Menezes PL, Kishore, Kailas S V., Lovell MR. Role of surface texture, roughness, and hardness on friction during unidirectional sliding. *Tribol Lett* 2011;41:1-15. <https://doi.org/10.1007/s11249-010-9676-3>.
48. Sen U. Wear properties of niobium carbide coatings performed by pack method on AISI 1040 steel. *Thin Solid Films* 2005;483:152-7. <https://doi.org/https://doi.org/10.1016/j.tsf.2005.01.008>.
49. Sen U. Friction and wear properties of thermo-reactive diffusion coatings against titanium nitride coated steels. *Mater Des* 2005;26:167-74. <https://doi.org/https://doi.org/10.1016/j.matdes.2004.05.010>.
50. Sen S, Sen U. Sliding wear behavior of niobium carbide coated AISI 1040 steel. *Wear* 2008;264:219-25. <https://doi.org/10.1016/j.wear.2007.03.006>.
51. Zhao H, Xie L, Xin C, Li N, Zhao B, Li L. Effect of molybdenum content on corrosion resistance and corrosion behavior of Ti-Mo titanium alloy in hydrochloric acid. *Mater Today Commun* 2023;34:105032. <https://doi.org/https://doi.org/10.1016/j.mtcomm.2022.105032>.
52. Guo RQ, Zhang C, Chen Q, Yang Y, Li N, Liu L. Study of structure and corrosion resistance of Fe-based amorphous coatings prepared by HVAF and HVOF. *Corros Sci* 2011;53:2351-6. <https://doi.org/https://doi.org/10.1016/j.corsci.2010.12.022>.
53. Zhang J, Liu J, Liao H, Zeng M, Ma S. A review on relationship between morphology of boride of Fe-B alloys and the wear/corrosion resistant properties and mechanisms. *J Mater Res Technol* 2019;8:6308-20. <https://doi.org/10.1016/j.jmrt.2019.09.004>.
54. Ma S, Xing J, Fu H, Yi D, Li Y, Zhang J, et al. Microstructure and interface characteristics of Fe-B alloy in liquid 0.25wt.% Al-Zn at various bath temperatures. *Mater Chem Phys* 2012;132:977-86. <https://doi.org/https://doi.org/10.1016/j.matchemphys.2011.12.044>.
55. Ma S, Xing J, Fu H, Yi D, Zhang J, Li Y, et al. Interfacial morphology and corrosion resistance of Fe-B cast steel containing chromium and nickel in liquid zinc. *Corros Sci* 2011;53:2826-34. <https://doi.org/https://doi.org/10.1016/j.corsci.2011.05.020>.
56. Ma S, Xing J, Fu H, Yi D, Zhi X, Li Y. Effects of boron concentration on the corrosion resistance of Fe-B alloys immersed in 460°C molten zinc bath. *Surf Coatings Technol* 2010;204:2208-14. <https://doi.org/https://doi.org/10.1016/j.surfcoat.2009.12.010>.
57. Abakay E, Sen U. Effect of Morphological and Microstructural Variations on the Properties of Electroless Nickel Boron Coatings. *Trans Indian Inst Met* 2023;76:657-64. <https://doi.org/10.1007/s12666-022-02754-8>.
58. Gu Z, Mao P, Gou Y, Chao Y, Xi S. Microstructure and properties of MgMoNbFeTi₂Y_x high entropy alloy coatings by laser cladding. *Surf Coatings Technol* 2020;402:126303. <https://doi.org/https://doi.org/10.1016/j.surfcoat.2020.126303>.
59. QIN L, LIAN J, JIANG Q. Effect of grain size on corrosion behavior of electrodeposited bulk nanocrystalline Ni. *Trans Nonferrous Met Soc China* 2010;20:82-9. [https://doi.org/https://doi.org/10.1016/S1003-6326\(09\)60101-1](https://doi.org/https://doi.org/10.1016/S1003-6326(09)60101-1).
60. Lu B, Luo J, Chiovelli S. Corrosion and wear resistance of chrome white irons---A correlation to their composition and microstructure. *Metall Mater Trans A* 2006;37:3029-38. <https://doi.org/10.1007/s11661-006-0184-x>.
61. Kocaman E, Kılıç B, Durmaz M, Şen S, Şen U. The influence of chromium content on wear and corrosion behavior of surface alloyed steel with Fe(16-x)Cr_x(B,C)4 electrode. *Eng Sci Technol an Int J* 2020. <https://doi.org/https://doi.org/10.1016/j.jestch.2020.08.003>.
62. Liu C, Liu Z, Gao Y, Wang X, Zheng C. Effect of Cr Content on Corrosion Resistance of Ni-xCr-Mo Laser-Cladding Coatings under H₂S-Induced High-Temperature Corrosion Atmosphere. *Materials (Basel)* 2022;15. <https://doi.org/10.3390/ma15051885>.

Disclaimer/Publisher's Note: The statements, opinions and data contained in all publications are solely those of the individual author(s) and contributor(s) and not of MDPI and/or the editor(s). MDPI and/or the editor(s) disclaim responsibility for any injury to people or property resulting from any ideas, methods, instructions or products referred to in the content.